On the Modeling of Light Interactions with Human Blood

D. Yim, G.V.G. Baranoski, T.F. Chen, B.W. Kimmel and E. Miranda

Natural Phenomena Simulation Group, D.R. Cheriton School of Computer Science, University of Waterloo
Technical Report CS-2011-30
December, 2011

Abstract

The development of predictive appearance models for organic tissues is a challenging task due to the inherent complexity of these materials. In this report, we closely examine the biophysical processes responsible for the appearance attributes of whole blood, one the most fundamental of these materials. We describe a new appearance model that simulates the mechanisms of light propagation and absorption within the cellular and fluid portions of this specialized tissue. The proposed model employs a comprehensive, and yet flexible first principles approach based on the morphological, optical and biochemical properties of blood cells. This approach allows for environment driven changes in the cells' anatomy and orientation to be appropriately included into the light transport simulations. The correctness and predictive capabilities of the proposed model are quantitatively and qualitatively evaluated through comparisons of modeled results with actual measured data and experimental observations reported in the scientific literature. Its incorporation into rendering systems is illustrated through images of blood samples depicting appearance variations controlled by physiologically meaningful parameters. Besides the contributions to the modeling of material appearance, the research presented in this report is also expected to have applications in a wide range of biomedical areas, from optical diagnostics to the visualization and noninvasive imaging of blood-perfused tissues.

1 Introduction

The realism of computer generated images is directly associated with the careful modeling of material appearance, *i.e.*, how different materials reflect, transmit and absorb light. Accordingly, one of the focal points of computer graphics research has been the development of light interaction models to enable the rendering of believable images of a wide range of man-made and natural materials. In recent years, substantial efforts have been directed toward the development of models that can also be used in a predictive manner [21], extending their scope of applications to other disciplines. For example, predictive models of light interaction with organic materials can be employed in the design of more effective diagnostic procedures and instruments [39, 18, 5, 70]. However, despite the remarkable progress that has been achieved in material appearance modeling [13], predictive solutions for fundamental organic materials remain elusive. In this report, we investigate the interactions of light with one of the most important of these materials, human blood, a highly specialized type of connective tissue in which cells are suspended and carried in a fluid called plasma.

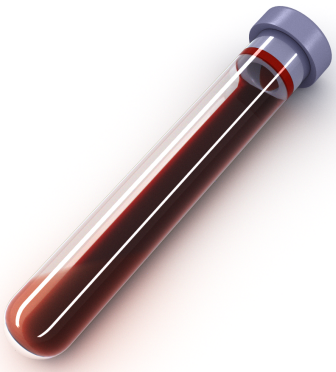

Figure 1: Image rendered using the proposed model of light interaction with human blood.

The spectral and spatial distributions of light incident on whole blood not only determine its appearance attributes (*e.g.*, color and translucency), but also provide crucial information about the medical condition of an individual. For example, the noninvasive optical monitoring of oxygen saturation, known as pulse oximetry, is arguably one of the most important methods for assessing the well-being and safety of patients during surgery, anesthesia recovery and critical care [15, 18]. Computations of light propagation in blood are also often performed to correlate theoretical results to measured values in order to determine changes to biochemical and morphological characteristics of blood triggered by pathological conditions [60, 18, 51]. Furthermore, the appearance of blood-perfused tissues are significantly affected by tissue blood content since the properties of whole blood itself are substantially different from those of soft tissues [75]. For these reasons, predictive simulations of light interactions with blood controlled by physiologically meaningful parameters are also of great importance for the imaging, screening, diagnosis and treatment of tissue disorders [39, 62, 5, 73].

In this report, we present a novel model for the predictive simulation of light interactions with blood. The proposed model employs a first principles approach that takes into account the specific morphological and optical properties of blood cells, to compute both the spectral (reflectance and transmittance) and spatial (scattering) responses associated to the appearance attributes of blood. Using this approach, the proposed cell-based model of light interaction with whole blood, herein referred to as the CLBlood model, can account for changes in the biophysical properties of blood cells and plasma under different physiological conditions and rheological states (stationary and steady flow). We remark, however, that our investigation focuses on light-matter interaction issues, *i.e.*, the modeling of blood flow dynamics is beyond the

scope of this work. Since our research is aimed not only at rendering applications, but also at biomedical applications, the CLBlood model is designed to provide multispectral predictions in the ultraviolet (UV), visible and near-infrared (NIR) regions of the light spectrum. The correctness of these predictions are quantitatively and qualitatively evaluated through detailed comparisons with actual measured data and observations of blood optical phenomena reported in the scientific literature. We also present images rendered using the CLBlood model to further illustrate its predictive capabilities and its use in realistic image synthesis.

The remainder of this report is organized as follows. The next section provides a concise review of related work in the biomedical and computer graphics fields. Section 3 provides an overview of blood optical properties that are essential for the modeling of its appearance attributes under different physiological and rheological conditions. Section 4 describes the CLBlood model. Section 5 outlines our evaluation procedures and provides the biophysical data set used in our simulations so that they can be seamlessly reproduced by computer graphics and biomedical researchers. Section 6 presents the evaluation results and discusses the predictive capabilities of the proposed model. Section 7 concludes the report and highlights directions for future work.

2 Related Work

In the biomedical field, models based on the Twersky's theory [3, 4, 37] and the diffusion theory [66, 64] and its approximations, such as the diffuse dipole [27] and multipole expansions [14], have been employed in the estimation of blood optical parameters. While models based on the original Twersky's thory do not describe the spatial distribution of the reflected and transmitted light [66], models based on the original diffusion theory provide valid approximations for light transport in a medium whose absorption coefficient is significantly smaller than its scattering coefficient [62]. However, this condition is not satisfied for blood in visible spectral domains. Numerical adding-doubling [55] and Monte Carlo methods [24] can overcome this limitation [75]. Accordingly, they have been applied in a number of inverse algorithms aimed at the determination of blood optical properties [49, 62, 74, 60, 18]. Recently, Monte Carlo methods have also been employed in the quantification of absorption flattening effects [50] and in two-dimensional simulations aimed at the NIR detection of blood coagulation [51]. In general, the accuracy of simulations based on these analytical and numerical approaches is limited by oversimplifications with respect to the scattering and absorption properties of blood components. For example, light is often assumed to traverse a blood cell without any internal reflections, which can result in significant deviations from the actual absorption profile of whole blood [33, 60]. Also, the collective scattering behavior of whole blood is often simulated using empirical phase functions or scattering theories that represent blood cells by cylinders, spheres or ellipsoids, and these approximations can lead to significant deviations from the actual scattering profile of whole blood [75, 31, 48, 72].

Few computer graphics related papers addressing the appearance of blood have been published to date. In visualization works aimed at applications in biology and medicine [26, 46, 61, 47, 53, 57], the appearance of blood is usually rendered using simplified color coded schemes. In realistic rendering applications, models of light interaction with human tissues (*e.g.*, [34, 12, 35]) account for the presence of blood through the incorporation of absorption coefficients of blood-borne pigments in the simulations. Although there are a number of detailed models aimed at the realistic rendering of fluid media (*e.g.*, [19, 22]) and particulate materials (*e.g.*, [67, 30, 28]), these models are not designed to account for specific morphological, optical and physiological factors affecting light interactions with blood cells. These factors are essential for the predictive modeling of whole blood appearance. Furthermore, to the best of our knowledge, none of the existing material appearance models accounts for rheological effects on the specific optical properties of material constituents. These effects can result in noticeable changes in the absorption and scattering profiles of whole blood [7, 39].

3 Blood Optical Properties

The cellular portion of blood is called formed elements, and it includes the erythrocytes or red blood cells (RBCs), the white blood cells (WBCs) and the platelets (PLTs) [11]. Although the volume fraction of human blood occupied by the formed elements, clinically known as the hematocrit and denoted by HCT, usually varies from 0.37-0.52, lower values can also be observed under *in vivo* conditions (*e.g.*, during heart surgery, the patient's hematocrit is usually lowered [44]), and may be lower than 0.01 under *in vitro* conditions (*e.g.*, during blood optics investigations and disease screening tests [75, 18]). The optical properties of human blood under normal physiological conditions are largely determined by light interactions with plasma and RBCs [75], which account for 99% of the formed elements [45]. The effects of the optical properties of WBCs and PLTs on the light scattering and absorption by whole blood are considered negligible [75, 44].

RBCs have a thin plasma membrane that encloses mainly a hemoglobin solution. The absorption and scattering of light by the RBCs are two to three orders of magnitude higher than those of the other blood components [45]. The light scattered by a single RBC depends on its shape, volume, refractive index and orientation [31]. Normal RBCs are characterized by a biconcave disk shape (Fig 2), with a volume, surface area and diameter ranging from $80 - 108\mu m^3$, $119 - 151\mu m^2$ and $7.2 - 8.44\mu m$ respectively [9, 75]. Their refractive index corresponds essentially to the refractive index of the hemoglobin solution due to the negligible thickness ($\approx 7nm$) of their membrane [69]. With respect to the angular distribution of the scattered light, the RBCs are characterized by a strong forward scattering behavior, with an average scattering angle about 5° [36] and an exponential fall-off [31].

The main morphological characteristics of the RBCs, such as the presence of concavities on their sides (minimum thickness $T_{min} = 0.81 \pm 0.35\mu m$ and maximum thickness $T_{max} = 2.58 \pm 0.27\mu m$ [9, 75]), make exact light scattering calculations difficult [72]. It has been demonstrated by theoretical studies [68, 72] and corroborated by recent experiments [31] that the use of simplified geometric representations for the RBCs, such as cylinders with rounded edges, spheres and ellipsoids, result in inaccurate scattering and absorption estimations. Environmental factors, however, may alter their shape, volume and refractive index. For example, when a RBC is exposed to a hypotonic solution, it may acquire water and swell.

The absorption of light by the RBCs is dominated by hemoglobin in its functional, oxygen-binding, forms [15], namely oxyhemoglobin and deoxyhemoglobin. Other types of hemoglobin that do not bind oxygen reversibly, known as dysfunctional hemoglobins, namely methemoglobin, carboxyhemoglobin and sulfhemoglobin, comprise less than 3% of the total hemoglobin content in healthy individuals [15, 25, 76]. It is worth noting that sulfhemoglobin is not normally present in the human body [20]. Water also plays a minor role in the absorption of light by RBCs, notably in the NIR range. Since RBCs are essentially a package of hemoglobin solution, the Beer-Lambert law can be employed

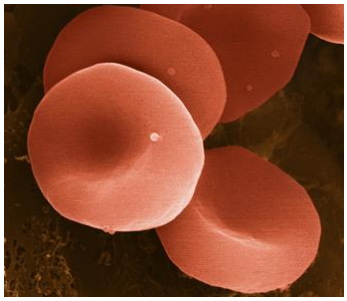

Figure 2: Color coded scanning electron micrograph of red blood cells. Image credits: Tina Carvalho/MicroAngela.

to quantify the absorption of light traveling within this solution [69]. It is necessary to take into account, however, that the optical path of light traveling within a cell may increase due to multiple reflections at its internal boundary [33, 60]. Hence, the amount of light absorbed within the RBC depends on the cell shape, orientation with respect to the incident light as well as its hemoglobin concentration and oxygen saturation level, SaO_2, which determines the fraction of oxyhemoglobin and deoxyhemoglobin.

It is important to note that the optical properties of whole blood differ markedly from those of hemoglobin solutions, which follow the Beer-Lambert law [33, 40, 54]. Light may traverse whole blood without encountering the RBCs, a phenomenon known as the sieve effect [54]. Alternatively, its optical path length may be increased due to the refraction between and within the RBCs, a phenomenon knwon as detour effect [8]. In whole blood, sieve effects may reduce the absorption of light by intracellular hemoglobin, while detour effects may increase it in comparison with the amount light absorbed by solutions in which the same concentration of hemoglobin is uniformly dispersed [33, 54]. The sieve effect is more pronounced for low hematocrit samples [54], while the detour effect is more pronounced in high hematocrit samples [40].

Pure plasma consists of approximately 90% water, 7-9% proteins (about 60% albumin, 36% globulin and 4% fibrinogen) with the balance being composed of electrolytes, metabolic intermediates, vitamins, nutrients and waste products [11]. RBCs may also release hemoglobin into plasma due to the damage of their membrane caused by mechanical or chemical impact, a process known as hemolysis [60]. Plasma absorption in UV to visible range is associated with the absorption due to chromophores found in proteins and other molecules, while in the NIR range its is dominated by water absorption. The scattering properties of pure plasma are mainly described by Rayleigh scattering of protein molecules [45]. Although plasma shows weak absorption and scattering behaviors when compared to the RBCs, it has a noticeable influence on the absorption profile of whole blood due to its refractive index differences with the RBCs. These differences may result in an increase of the path length of light traversing the RBCs[60], which, in turn, increase the probability of light being absorbed within these cells.

The scattering and absorption properties of whole blood are significantly affected by its motion state measured in terms of its shear rate, which is defined as the velocity gradient in the direction normal to the flow [39]. At low shear rates, the cells are randomly oriented. As shear rate increases, many randomly oriented cells start to exhibit angular rotation (rolling or tumbling) and align with the major axis parallel to the flow direction. Although the degree of alignment increases with the shear rate, it also depends on the hematocrit. At high shear rates and high hematocrit (above 0.4), the alignment becomes more pronounced and the cells start to show some degree of elongation [7, 39].

4 The CLBlood Model

The proposed model employs a first principles simulation framework in which light is represented by discrete rays, each one traveling at a given wavelength λ. Within this framework, the interactions of light with plasma and individual cells are modeled as a random walk process. Scattering and absorption events are probabilistically accounted for using data driven procedures and wave optics resources when appropriate.

The CLBlood simulation pipeline can be divided into four main stages: cell representation, plasma-light interactions, cell positioning and cell-light interactions. These stages are implemented using Monte Carlo methods that rely on the generation of random numbers ξ_i, for $i = 1, 2, ..., 9$, uniformly distributed in the interval $[0, 1]$. The following description of this pipeline concentrates in the red blood cells due their dominant optical role. The interactions of light with other cells, such as WBCs and PLTs, can be handled similarly to the RBCs and are implicitly addressed in the model formulation by analogy.

4.1 Cell Representation

When a ray hits a cell, it can be reflected back to the surrounding medium or transmitted to the cell interior. In order to compute the probabilities of light reflection and absorption by a cell, we need a geometrical representation that can closely approximate its shape under different conditions. Furthermore, this representation needs to support operations performed during the subsequent simulation stages, namely the calculation of the cell volume and cross-sectional area (in the direction perpendicular to the ray propagation direction), the computation of ray-cell (internal boundary) intersections and the selection of random points on the surface of the cell facing the ray propagation direction.

Accordingly, we created a parametric NURBS representation [42] for the red blood cells (Figure 3). This representation allows us to accurately perform the required operations and effectively handle changes in the cells' morphology such as elongation and swelling. We used the biconcave cross-section profile of an unstressed red blood cell [65] to adjust the control points of the NURBS representation in order to have its volume and diameter within the typical range of normal RBCs. Standard rejection sampling techniques were then used to calculate the volume and the cross-sectional area of our *in silico* cells. Please refer to Appendix A for details about the use of this technique.

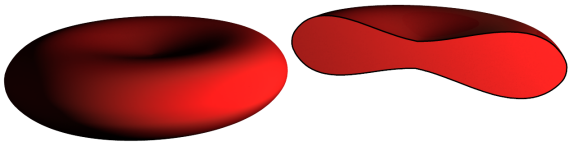

Figure 3: Sketch depicting the NURBS representation of biconcave red blood cells employed by the CLBlood model. Left: whole volume. Right: cross section.

4.2 Plasma-Light Interactions

When a ray first interacts with a blood volume, a standard Fresnel test is performed taking into account the angle of incidence of the incoming light and the refractive index differences of the surrounding medium and plasma. This test consists in computing the Fresnel coefficient, F, at the interface between the two media using the Fresnel equations [5], and comparing it with a random number ξ_1. If $\xi_1 \leq F$, then the ray is reflected back to the surrounding medium. Otherwise, it is transmitted to the fluid portion of blood where it may travel a distance d before hitting another interface with the surrounding medium or a cell. In both cases, Fresnel tests are performed to determine the next step in the random walk process. The computation of the distance d and the Fresnel tests involving the cells are described in the next sections.

A ray traversing a distance d in the plasma may be subject to scattering and absorption events. To account for scattering caused by protein molecules, we initially compute the Rayleigh scattering coefficient [43]:

$$\mu_s(\lambda) = \frac{128\pi^5 r^6 (c/M)}{3\lambda^4} \left(\frac{(\eta_p/\eta)^2 - 1}{(\eta_p/\eta)^2 + 2} \right)^2 \tag{1}$$

where η, c, r, and M respectively represent the refractive index, concentration, molecular radius and weight of each type of protein, and η_p corresponds to the refractive index of plasma. We then employ $\mu_s(\lambda)$ to compute the Rayleigh scattering probability for each type of protein using [55]:

$$P_{\mu_s}(\lambda) = 1 - e^{-\mu_s(\lambda)d}. \tag{2}$$

Finally, if $\xi_2 < P_{\mu_s}(\lambda)$, then the ray direction is perturbed according to the Rayleigh scattering phase function [55]. For simplicity, this perturbation is implemented using rejection sampling as shown in Algorithm 1, where θ_R represents the polar perturbation angle, and ϕ_R corresponds to the azimuthal perturbation angle.

Algorithm 1 Rejection sampling for Rayleigh scattering.

$\phi_R \leftarrow 2\pi\xi_3$
repeat
  $\theta_R \leftarrow \pi\xi_4$
until $\xi_5 \leq \left(\frac{3\sqrt{6}}{8}\right)(1 + \cos^2\theta_R)\sin\theta_R$
return (θ_R, ϕ_R)

To compute the absorption probability, we employ a stochastic representation of the Beer-Lambert law [55]:

$$P_{\mu_{a_p}}(\lambda) = 1 - e^{-\mu_{a_p}(\lambda)d}, \tag{3}$$

where $\mu_{a_p}(\lambda)$ corresponds to the effective absorption coefficient of plasma. After $P_{\mu_{a_p}}(\lambda)$ is computed, the testing is performed, *i.e.*, if $\xi_6 < P_{\mu_{a_p}}(\lambda)$, then the ray is terminated.

4.3 Cell Positioning

The human blood has approximately 5×10^6 red blood cells per mm^3 [11]. This makes the construction of the entire geometrical layout of the cells beforehand impractical. For this reason, in the CLBlood model, we generate the cells on the demand, *i.e.*, a cell is probabilistically positioned in the blood volume to enable the simulation of its interactions with light. After the simulation is performed, the cell is discarded, and the process is repeated for the next cell (Figure 4). Hence, using this instantiation strategy, previously employed in the simulation of light transport in sand [30], we can explicitly account for cell-light interactions without having to store them.

When a ray is traversing through plasma, we first probabilistically determine the distance d that the ray travels before hitting a cell. Its computation takes into account the distribution and the volume occupied by cells in the medium as well as their orientation. This is essential for the convergence of the model predictions to the same results that would have been obtained if the entire layout of the cells were geometrically assembled. Accordingly, the distance d is computed using the following expression [30]:

$$d = -\frac{1}{K(\vec{\omega})} \log \xi_7, \tag{4}$$

where $K(\vec{\omega})$ represents the cross-sectional area of the RBCs per unit volume given a ray traveling in a direction $\vec{\omega}$. This parameter can be further separated into two components depicted in the following integral over all possible orientations of the RBCs in the blood volume:

$$K(\vec{\omega}) = \int_{\vec{u}} n(\vec{u}) G(\vec{u}, \vec{\omega}) \mathrm{d}\vec{u}, \tag{5}$$

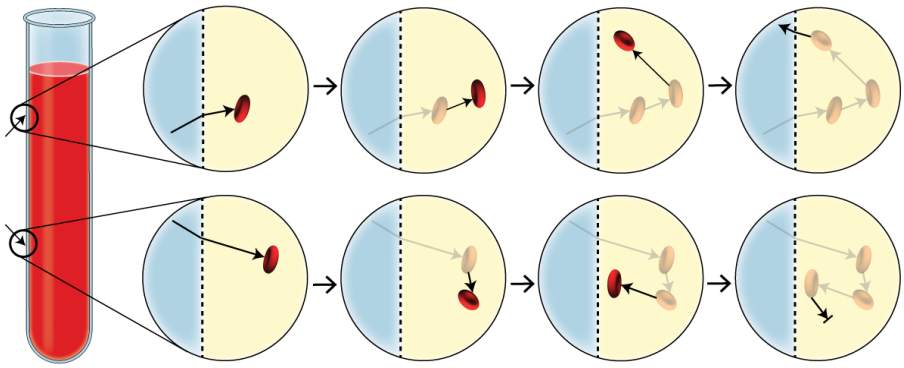

Figure 4: Sketch illustrating possible paths that can be followed by a ray traversing a blood sample in which the cells are probabilistically positioned on demand during the simulations, and then discarded. Top: light returns to the surrounding medium. Bottom: light is absorbed.

where $n(\vec{u})$ represents the number of RBCs per unit volume with the orientation given by $\vec{u}$, and $G(\vec{u},\vec{\omega})$ corresponds to the cross-sectional area of an RBC with an orientation $\vec{u}$ and exposed to the direction $\vec{\omega}$ of the current ray. If the cells are assumed to be randomly oriented, *i.e.*, all possible orientations have equal probability, then the parameter $n(\vec{u})$ is reduced to $HCT/(4\pi\ MVC)$, where MVC represents the mean volume of the RBCs. For notation simplicity, we represent the ratio HCT/MVC by δ in the remainder of this section.

The formula for $G(\vec{u},\vec{\omega})$ depends on the shape of the cell being used. Considering the NURBS representation used for our *in silico* cells, $G(\vec{u},\vec{\omega})$ is given by:

$$G(\vec{u},\vec{\omega}) = \frac{1}{2}(\gamma_1(1-|\cos\psi|)+\gamma_2|\cos\psi|), \tag{6}$$

where γ_1 and γ_2 are the cross-sectional areas of the *in silico* cells viewed from the side and the top respectively, and ψ corresponds the angle between the direction of the ray, $\vec{\omega}$, and the direction that the top of the cell is facing. For the sake of conciseness, derivation details are provided in Appendix B. Hence, in the case in which all possible cell orientations have an equal probability, $K(\vec{\omega})$ can be analytically expressed as:

$$K_{random} = 0.5\,(\gamma_1+\gamma_2)\,\delta. \tag{7}$$

Recall that during steady flow the cells are likely to have a rolling distribution (Section 3). We remark that $G(\vec{u},\vec{\omega})$ is given by Equation 6. Since in this case the cells are rotating with respect to an axis defined by a vector $\vec{a}$, we have $n(\vec{u}) = \delta/2\pi$, which gives:

$$K_{rolling}(\vec{\omega}) = \delta\gamma_1(1-|\sin\beta|) + \frac{\delta}{2\pi}(\gamma_1(2\pi-4)+4\gamma_2)|\sin\beta|), \tag{8}$$

where β is the angle between $\vec{\omega}$ and $\vec{a}$.

Under high shear rate conditions, the cells are likely to be horizontally aligned with the flow (Section 3). In this case, the calculation of the cross-sectional area per unit volume becomes simpler. We assume that that a horizontally aligned cell has its major axis on the X-Y plane. Also, since all the cells are oriented the same way, we have $n(\vec{u},\vec{\omega}) = \delta$, which gives:

$$K_{aligned}(\vec{\omega}) = \delta(\gamma_1(1-|\cos\psi|)+\gamma_2|\cos\psi|). \tag{9}$$

Once the distance d is computed, the orientation of the cell is selected by sampling the probability distribution functions (PDFs) associated with the orientations that were considered while generating the distance. The PDFs for the three orientation cases were derived (Appendix C) such that orientations that have a larger $G(\vec{u},\vec{\omega})$ have a higher probability of being selected. As described by Kimmel [29], the general expression for the PDF is the given by:

$$p(\vec{u}) = \frac{1}{K}n(\vec{u},\vec{\omega})G(\vec{u},\vec{\omega}) = \frac{n(\vec{u},\vec{\omega})G(\vec{u},\vec{\omega})}{\int_{\vec{u}} n(\vec{u},\vec{\omega})G(\vec{u},\vec{\omega})\mathrm{d}\vec{u}}. \tag{10}$$

In the three orientation distribution cases considered in this work, $n(\vec{u},\vec{\omega})$ is a constant, which results in:

$$p(\vec{u}) = \frac{G(\vec{u},\vec{\omega})}{\int_{\vec{u}} G(\vec{u},\vec{\omega})\mathrm{d}\vec{u}}. \tag{11}$$

Using Equation 11, we can obtain the PDFs for the three orientation distribution cases considered in our simulations, namely random, rolling and aligned, which are presented in the remainder of this section. Their derivation details are provided in Appendix C.

In the random case, the PDF is given by:

$$p_{random}(\psi,\phi) = \left(\frac{\gamma_1(1-|\cos\psi|)+\gamma_2|\cos\psi|}{\gamma_1+\gamma_2}, \frac{1}{2\pi}\right), \tag{12}$$

where ψ and ϕ correspond respectively to the polar and azimuthal angles with respect to the ray direction $\vec{\omega}$.

In the case where the cells are rolling around an axis $\vec{a}$, we know that the orientation is mostly fixed except for determining how much the cell is rotated with respect to $\vec{a}$. The PDF in this case is then given by:

$$p_{rolling}(\theta) = \frac{\chi + (\gamma_1(1 - |\cos\theta|) + \gamma_2|\cos\theta|)|\sin\beta|}{2\pi\chi + |\sin\beta|[\gamma_1(2\pi - 4) + 4\gamma_2]}, \tag{13}$$

where θ is the rotation angle and $\chi = \gamma_1(1 - |\sin\beta|)$.

In the case where all cells are aligned, they all must have the same orientation $\vec{U}$. Hence, if $\vec{u} = \vec{U}$, then the PDF is given by $p_{aligned}(\vec{u}) = 1$. Otherwise, it is given by $p_{aligned}(\vec{u}) = 0$.

Finally, we randomly pick the hitting point on the cell surface among the set of points facing the ray. After the position, orientation and hitting point are selected, the model simulates the cell-light interactions as described in the next section.

4.4 Cell-Light Interactions

When the light hits a cell, we initially determine whether it is reflected or enters the cell by performing a Fresnel test using the refractive index differences between plasma and the hemoglobin solution within the cell. If the light enters the cell, we test whether it is absorbed by generating a random number ξ_7 and comparing with the probability of light absorption within the cell given by $P_{\mu_{a_s}}(\lambda,)$, where μ_{a_s} represents the effective absorption coefficient of the solution inside the cell. If $\xi_7 < P_{\mu_{a_s}}(\lambda)$, then the ray is terminated. Otherwise it is scattered.

Although the absorption probability can be computed on the fly, performance improvements are obtained by pre-computing it offline since the same operations are repeated for all cells. In this case, the $P_{\mu_{a_s}}(\lambda)$ values are stored in a table indexed by wavelength and the incidence geometry of the incident light, *i.e.*, the intersection point x and the angle of incidence θ_i with respect to the cell's normal vector at this point. Due to the overall symmetry of the RBCs, only a small number of points need to be taken into account in order to obtain asymptotically convergent results in the simulations. For example, the results provided in Section 6 were obtained considering seven points and an angular resolution of 2°.

The probability of absorption $P_{\mu_{a_s}}(\lambda)$ is computed by simulating the interactions of light inside the cell. Once a ray penetrates the cell, we compute its intersection point with the internal surface of the *in silico* cell using a practical ray-NURBS intersection algorithm[42]. At each intersection point, a Fresnel test is performed to determine whether the ray exits the cells or continues to bounce inside it. The termination of a ray due to light absorption between each bounce is also probabilistically determined using the Beer-Lambert law [55]:

$$P^r_{\mu_{a_s}}(\lambda) = 1 - e^{-\mu_{a_s}(\lambda)d_c}, \tag{14}$$

where d_c corresponds to the distance traveled by the ray within the cell, *i.e.*, between bounces. The effective absorption coefficient of the solution inside the the cell can be expressed as:

$$\mu_{a_s}(\lambda) = c_f((SaO_2)\varepsilon_{oh}(\lambda) + (1 - SaO_2)\varepsilon_{dh}(\lambda)) + c_d(\varepsilon_{mh}(\lambda) + \varepsilon_{ch}(\lambda) + \varepsilon_{sh}(\lambda)) + \alpha(\lambda), \tag{15}$$

where c_f and c_d represent the concentration of the functional and dysfunctional hemoglobins; $\varepsilon_{oh}(\lambda)$, $\varepsilon_{dh}(\lambda)$, $\varepsilon_{mh}(\lambda)$, $\varepsilon_{ch}(\lambda)$ and $\varepsilon_{sh}(\lambda)$ correspond to the extinction coefficients of oxyhemoglobin, deoxyhemoglobin, methemoglobin, carboxyhemoglobin and sulfhemoglobin, respectively; and $\alpha(\lambda)$ is the absorption coefficient of water. After $P^r_{\mu_{a_s}}(\lambda)$ is computed, the absorption testing is performed, *i.e.*, if $\xi_8 < P^r_{\mu_{a_s}}(\lambda)$, then the ray is terminated. For the offline pre-computations mentioned above, this process is repeated for m rays. For example, the simulation results presented in Section 6 were obtained using $m = 10^6$.

If the ray is scattered by the cell, its direction of propagation is perturbed using a data driven approach based on measurements of angular scattering distributions performed for single RBCs [31]. Accordingly, the polar perturbation angle θ_s is randomly selected from an exponential scattering distribution with a mean of 5° [36], while the azimuthal perturbation angle ϕ_s is randomly selected assuming an azimuthal symmetry, *i.e.*, $\phi_s = 2\pi\xi_9$.

5 Evaluation Framework

The predictions provided by the CLBlood model were quantitatively and qualitatively evaluated through comparisons of modeled data with actual measured data [23, 44, 74] and experimental observations provided in the biomedical literature [33, 7, 39, 40, 64, 54]. In this section, we describe the steps taken so that the actual measurements conditions were reproduced as faithfully as possible in our *in silico* experiments. We also provide the values assigned for user specified parameters and the sources for the "fixed" biophysical quantities that are not normally subject to change in the simulations.

The actual measured data employed in our quantitative comparisons was obtained by placing fully oxygenated blood samples ($SaO_2 = 1.0$) inside fused quartz cuvettes. In the case of the measured spectral reflectance data, Meinke *et al.* [44] employed a integrating sphere spectrophotometer and placed the cuvette at an angle of 8° to the incident light to exclude the Fresnel reflectance of the cuvette and measure only the diffuse directional-hemispherical reflectance. In the case of the measured scattering distribution data, Yarolavsky *et al.* [74] and Hammer *et al.*, [23] employed a goniophotometer and placed the cuvette at an angle of 0° to the incident light. The measurements of the intensity distribution of the scattered light were taken in the range from 2.5°-175° and reported as normalized intensity values in arbitrary units (a.u.). The corresponding modeled data was obtained employing the same experimental set-ups used in the actual measurements, which were reproduced using a virtual spectrophotometer and a virtual goniophotometer [5]. The modeled spectral curves used in our qualitative comparisons, unless otherwise stated, were also obtained considering a directional-hemispherical geometry and an angle of incidence of 8°. It is worth noting that the scattering intensity measurements performed by Hammer *et al.* were normalized above one, and the measurements performed by Yarolavsky *et al.* do not include values between 80° and 100°. These aspects were also taken into account in the plotting of the modeled and measured scattering profiles.

In the actual experiments performed by Meinke *et al.* [44] a $0.116mm$ thick cuvette was employed. They also measured the MVC of the RBCs in their blood samples, which was reported to be $83\mu m^3$. Unless otherwise stated, the same values were used in our *in silico* experiments, along with a cell diameter of $8.21\mu m$ [75] and a cell hemoglobin content equal to $29.5pg$ [38]. A 2% hemolysis was observed in the actual reflectance measurements by Meinke *et al.* [44] and incorporated in the computation of the corresponding modeled reflectance data used in our quantitative comparisons. For the fixed spectral quantities used in our simulations, namely the molar extinction coefficients of oxyhemoglobin and deoxyhemoglobin (Figure 5), the specific absorption coefficient of water (Figure 6), the effective absorption coefficient of plasma (Figure 7) as well as the refractive indices of hemoglobin and fused quartz (Figure 8), we employed spectral curves available in the literature. The curve for the plasma refractive index (Figure 9 used in our experiments corresponds to a 91% solution in which the concentrations of albumin, globulin and fibrinogen are $4.6g/L$, $2.6g/L$ and $0.38g/dL$ respectively [41]. Average values for the refractive indices of albumin, globulin and fibrinogen were also obtained using data available in the literature, 1.514 [1], 1.511 [1] and 1.563 [2] respectively, as well as values for thir molecular weights and molecular radii, which correspond to $1.13 \times 10^{-19}g/molecule$ [63], $2.7nm$ [32]; $1.62\times10^{-19}g/molecule$ [10], $2.95nm$ [10]; and $5.65\times10^{-19}g/molecule$ [59], $10.8nm$ [59], respectively. For experiments involving hemolysis, the effective absorption coefficient of plasma was adjusted to take into account light absorption by hemoglobin. Since the presence of dysfunctional hemoglobins was not reported in the actual experiments, they were not included in the corresponding simulations either. However, the effects of methemoglobin and sulfhemoglobin on the appearance of whole blood samples were illustrated through images rendered using the proposed model and considering their molar extinction coefficients (Figure 10).

The rheological states in which the actual experiments were performed were also taken into account in our simulations. Unless otherwise stated, for experiments performed in a stationary (suspension) state, the RBCs were assumed to be randomly oriented (Section 3). Since the experiments by Meinke *et al.* [44] were performed under steady flow and high shear rate conditions, we considered the RBCs to be either randomly oriented with angular rotation (30%) or aligned with the flow (70%) in the corresponding simulations. These figures were selected considering experimental work [39] performed under similar rheological conditions. Since the actual measured reference data used in the quantitative comparisons was obtained either for samples with HCT below 0.4 or in a stationary (suspension) state, cell elongation was not considered in those comparisons.

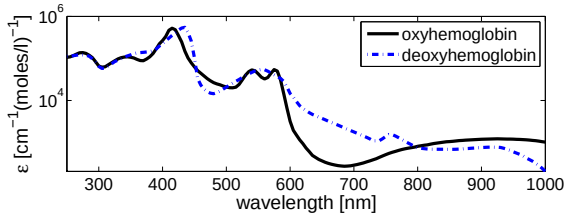

Figure 5: Molar extinction coefficient curves for oxyhemoglobin and deoxyhemoglobin [56].

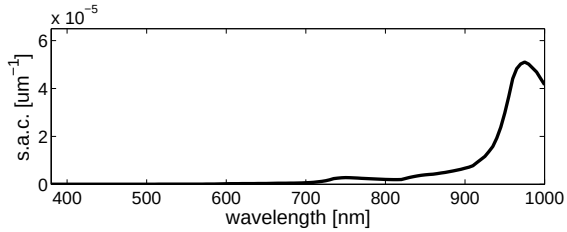

Figure 6: Specific absorption coefficient (s.a.c.) curve for water [52].

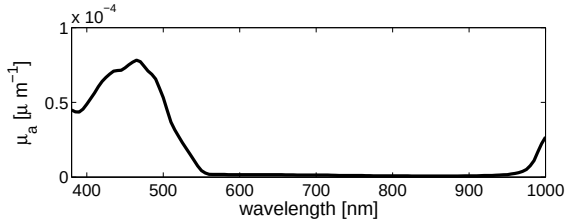

Figure 7: Effective absorption coefficient curve for plasma [45].

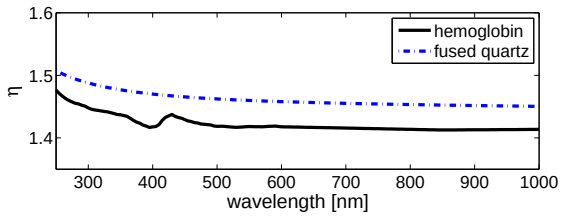

Figure 8: Refractive index curves for hemoglobin [17] and fused quartz [6].

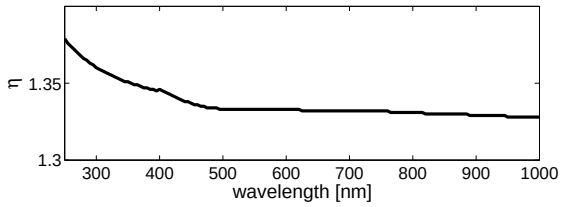

Figure 9: Refractive index curve for plasma [1, 52].

6 Results and Discussion

Figure 11 presents comparisons of modeled reflectance curves with actual measured curves provided by Meinke *et al.* [44] for different HCT values. These comparisons show that the shapes of the modeled curves closely agree with the shapes of their measured counterparts. As demonstrated in the latter, below $600nm$, a region where absorption prevails over scattering [44], the reflectance of blood increases with decreasing HCT, while above $600nm$, it decreases. As it can be observed in Figure 11, the modeled curves can correctly reproduce this behavior. The comparisons depicted in Figure 11 also indicate a close quantitative agreement between the modeled and measured curves, especially considering that certain biochemical and biophysical input parameters, such as hemoglobin content and cell diameter, correspond to averaged data. It is also worth noting that Meinke *et al.* mentioned the possibility of minor instrument and preparation errors in the reference measurements.

Figure 12 presents comparisons of scattering intensity profiles provided by the CLBlood model with actual scattering intensity profiles measured by Hammer *et al.* [23] and Yarolavsky *et al.* [74] below and above $600nm$ respectively. These comparisons reveal a close quantitative and qualitative agreement between the model predictions and the measured data, demonstrating that the strong forward scattering behavior of whole blood is captured by the proposed model.

The two functional hemoglobin forms, oxyhemoglobin and deoxyhemoglobin, have the same molar extinction coefficient around $800nm$, their isosbestic point [75]. By reducing the level of oxygenation, the reflectance decreases for wavelengths below this point, and increases for wavelengths above it as demonstrated in experiments by Meinke *et al.* [44]. Experiments by Serebrennikova *et al.* [64] also show that a dramatic reduction of the level of oxygenation results not only in the flattening of the characteristic oxyhemoglobin "w" signature between $500nm$ to $600nm$, but also in a significant enhancement in the reflectance peak around $480nm$ and in the reflectance dip around $760nm$. The curves presented in Figure 13 indicate that the CLBlood model captures this non-trivial behavior of the functional hemoglobins, which provides the basis for noninvasive optical monitoring procedures such as pulse oximetry. This behavior is also responsible by the distinct bright red appearance of oxygenated (arterial) blood in comparison with the dark red appearance of deoxygenated (venous) blood [15], which are illustrated in the images presented in Figure 14.

Recall that motion may affect the properties of red blood cells, and consequently how light is reflect and transmitted by flowing blood. Experiments described in literature [7, 39] show that as the shear rate increases, the RBCs start to align with their major axis parallel to the flow direction. This change of orientation, in turn, increases light reflection and reduces light transmission. We have performed simulations to examine the predictive capabilities of the CLBlood model with respect to these effects. As can be observed in Figure 15, the results of our *in silico* experiments are consistent with the reflection and transmission changes observed in the experiments reported in the literature.

We remark that the optical properties of whole blood differ markedly from those of hemoglobin solutions due to sieve and detour effects [33, 54, 40]. While the former reduces absorption (notably in bands of absorption maxima), the latter increases absorption (notably in bands of absorption minima) [60, 50, 5]. For samples with low hematocrit, the net result of these phenomena is a reduction in the amount of light absorbed by whole blood in comparison with the amount of light absorbed by solutions in which the same concentration of hemoglobin is uniformly dispersed (*e.g.*, completely hemolysed blood samples) [54], while for samples with a high hematocrit, the net result is an increase in the amount of light absorbed by whole blood [40]. Figure 16 depicts the results of our *in silico* experiments involving a fully hemolysed blood suspension and a whole blood suspension composed of intact cells. As indicated in the graphs, the cell-based design of the CLBlood model correctly incorporates sieve and detour effects responsible for the distinct appearances of whole blood and hemoglobin solutions. These distinct appearances are further illustrated in the images presented in Figure 17.

Besides its connection with oxygen saturation levels, the blood color is also a diagnostic pointer for serious medical conditions associated with the excess of dysfunctional hemoglobins in the blood, such as methemoglobinemia and sulfhemoglobinemia, usually caused by a drug reaction [76, 20]. Large amounts of these dysfunctional hemoglobins may give blood a chocolate-brown appearance [25, 20, 71, 76]. These abnormal chromatic attributes of blood are illustrated in the images presented in Figure 18.

Finally, Figures 1 and 19 present rendered images to further illustrate appearance variations associated with different physiological parameters. From a visual perspective, HCT and SaO_2 are the most important model parameters considering samples with the same thickness

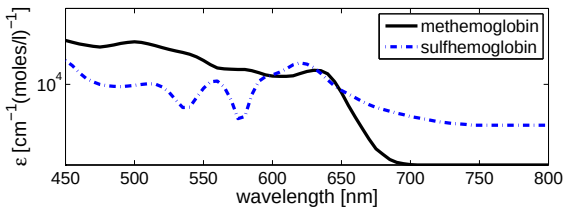

Figure 10: Molar extinction coefficient curves for methemoglobin [58] and sulfhemoglobin [76].

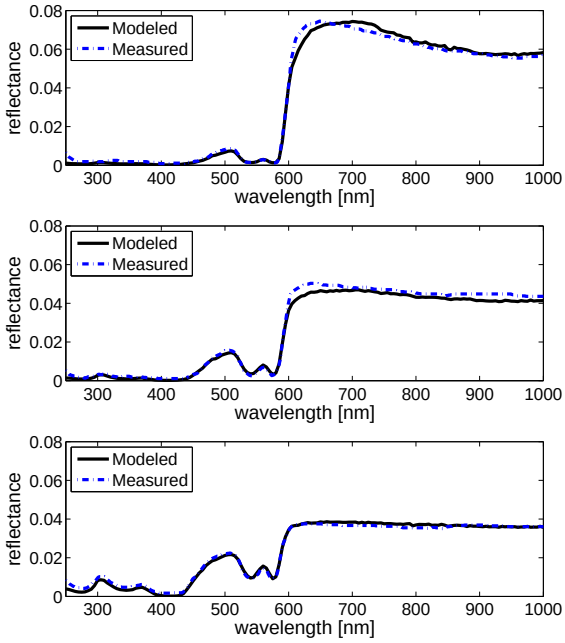

Figure 11: Comparison of modeled reflectance curves provided by the CLBlood model with curves measured by Meinke *et al.* [44] under steady flow conditions. Top: $HCT = 0.33$. Center: $HCT = 0.17$. Bottom: $HCT = 0.084$.

and under the same rheological conditions. Note that variations on thickness may also result in noticeable (visual) appearance changes as depicted in Figure 1 ($HCT = 0.4$ and $SaO_2 = 0.7$). The rendering of the images (1536×1152 pixels) presented in Figures 1 and 19 took $\approx 4.5h$, while the rendering of the remaining smaller images (768×576 pixels, before cropping) took $\approx 2h$ on a dual 6 core Intel Xeon X5650 processors ($2.66GHz$) with 24GB RAM.

7 Conclusion and Future Work

We have described the first predictive model of light interaction with human blood presented in the computer graphics literature. The CLBlood model provides spectral and scattering responses for blood samples under a wide range of physiological and rheological conditions. The model predictions have been evaluated through *in silico* experiments, and the results of these experiments show a close quantitative and qualitative agreement with actual measured data and experimental observations reported in the biomedical literature.

Despite the comprehensive first principles approach employed in the design of the CLBlood model, only a small set of physiologically meaningful parameters, such as the hematocrit and the oxygen saturation level, are required to predictively control the rendering of blood samples with distinct appearances. We remark that most of the biophysical quantities employed in the simulations, such as refractive indices and absorption coefficients, are not normally subject to change, and, therefore, can be kept fixed during rendering.

Due to their stochastic nature, the simulations performed by the CLBlood model are time consuming. However, alternatives exist to enhance their accuracy to cost ratio. For example, several stages of the simulation pipeline can be effectively executed offline, and their results stored and directly accessed during rendering time.

In our future work, we intend to explore several open avenues for interdisciplinary theoretical and applied research involving the diagnosis of medical conditions through blood spectral signatures. For example, several diseases related to the abnormal occurrence of dysfunctional hemoglobins can change the color of blood and blood-perfused tissues dramatically. We also intend to investigate the effects of extreme flow and abnormal physiological conditions on the cellular anatomy, and, consequently, on the appearance of whole blood and blood-perfused tissues.

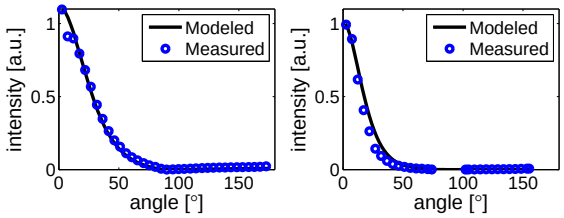

Figure 12: Comparison of modeled scattering intensity profiles provided by the CLBlood model with actual scattering intensity profiles measured at $514nm$ by Hammer *et al.* [23] and at $633nm$ by Yarolavsky *et al.* [74] for blood suspensions with $HCT = 0.4$ and $HCT = 0.38$, respectively. Left: $514nm$. Right: $633nm$.

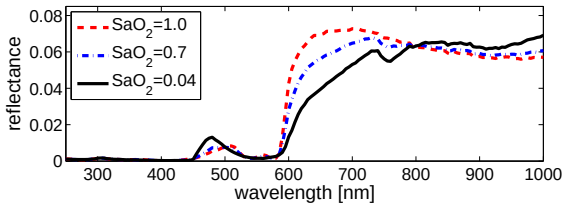

Figure 13: Comparison of modeled reflectance curves provided by the CLBlood model considering different levels of oxygenation (SaO_2) in whole blood suspensions with $HCT = 0.4$.

References

[1] ADAIR, G., AND ROBINSON, M. The specific refraction increments of serum-albumin and serum-globulin. *Biochem. J. 24*, 4 (1930), 993–1011.

[2] ANDERSEN, M., AND NIR, S. Van der waals parameters, refractive indices and dispersion equations of spectrin, actin and other mammalian proteins. *Polymer 18*, 9 (1977), 867–870.

[3] ANDERSON, N., AND SEKELJ, P. Light-absorbing and scattering properties of nonhaemolysed blood. *Phys. Med. Biol. 12*, 2 (1967), 173–184.

[4] ANDERSON, N., AND SEKELJ, P. Reflection and transmission of light by thin films of nonhaemolysed blood. *Phys. Med. Biol. 12*, 2 (1967), 185–192.

[5] BARANOSKI, G., AND KRISHNASWAMY, A. *Light and Skin Interactions: Simulations for Computer Graphics Applications*. Morgan Kaufmann, Elsevier, Burlington, MA, USA, 2010.

[6] BASS, M. *Handbook of Optics*, vol. 4. McGraw-Hill, New York, NY, USA, 2010.

[7] BITBOL, M. Red blood cell orientation in orbit C=0. *Biophys. J. 49* (1986), 1055–1068.

[8] BUTLER, W. Absorption spectroscopy in vivo: theory and application. *Annual Review of Plant Physiology 15* (1964), 451–470.

[9] CANHAM, P., AND BURTON, A. Distribution of size and shape in populations of normal red cells. *Circulation Research 422* (1968), 405–422.

[10] CORVOL, P., CHRAMBACH, A., RODBARD, D., AND BARDIN, C. Physical properties and binding capacity of testosterone-estradiol-binding globulin in human plasma, determined by polyacrylamide gel electrophoresis. *J. Biol. Chem. 246*, 11 (1971), 3435–3443.

[11] DE GRAAFF, K. V. *Human Anatomy*, 4th ed. Wm. C. Brown Publishers, Dubuque, IO, USA, 1995.

[12] DONNER, C., AND JENSEN, H. A spectral BSSRDF for shading human skin. In *17th Eurographics Workshop on Rendering* (2006), pp. 409–418.

[13] DORSEY, J., RUSHMEIER, H., AND SILLION, F. *Digital Modeling of Material Appearance*. Morgan Kaufmann/Elsevier, Burlington, MA, USA, 2008.

[14] EATON, G., VEITCH, A., NISBET, R., AND TURNBULL, F. The theory of the back-scattering of light by blood. *J. Phys. D:Appl. Phys. 11* (1978), 1463–1479.

[15] FLEWELLING, R. Noninvasive optical monitoring. In *The Biomedical Engineering Handbook* (Boca Raton, FL, USA, 1995), J. Bronzino, Ed., IEEE Press, pp. 1346–1356. Chapter 88.

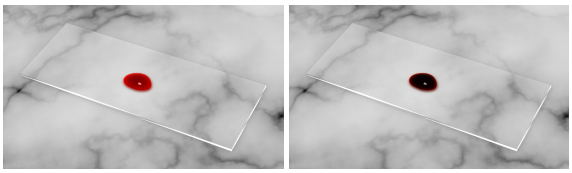

Figure 14: Images of blood droplets ($HCT = 0.4$) on a microscope slide showing spectral variations due to different oxygenation levels. Left: oxygenated (arterial) blood. Right: deoxygenated (venous) blood.

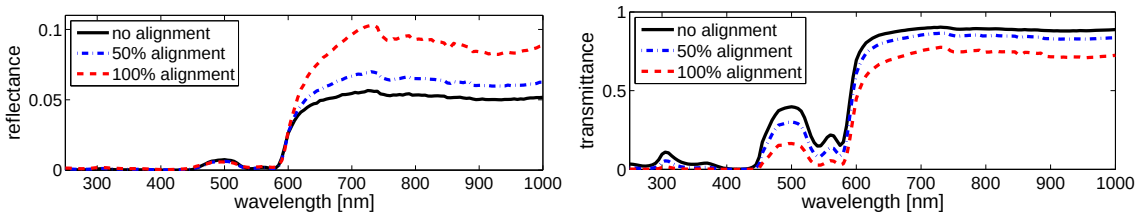

Figure 15: Comparison of modeled spectral curves considering different levels of RBC alignment for a blood sample ($HCT = 0.4$ and $SaO_2 = 0.7$) under steady flow conditions. Left: reflectance. Right: transmittance.

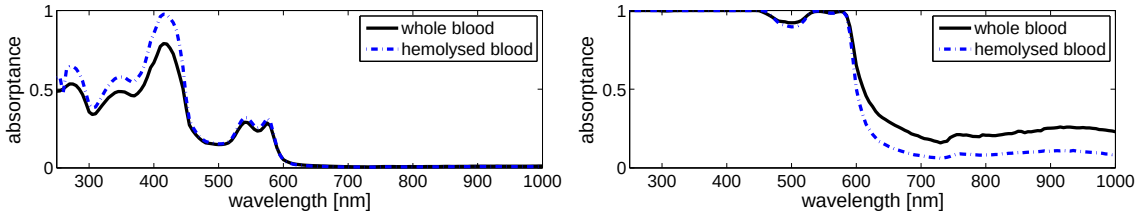

Figure 16: Comparison of modeled absorptance curves provided by the CLBlood model considering fully hemolysed and whole blood (intact cells) suspensions. Left: $HCT = 0.05$ and $SaO_2 = 0.7$. Right: $HCT = 0.4$ and $SaO_2 = 0.7$.

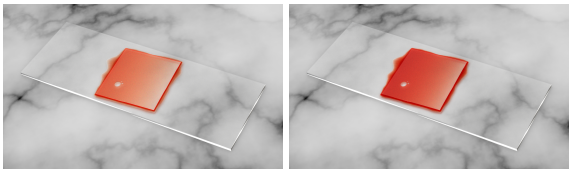

Figure 17: Images of blood samples under a microscope slide chip illustrating the appearance differences between hemolysed blood and whole blood. Both samples have $HCT = 0.4$ and $SaO_2 = 0.7$. Left: fully hemolysed sample. Right: whole blood (intact cells).

[16] FOLEY, J., VAN DAM, A., FEINER, S., AND HUGHES, J. *Computer Graphics: Principles and Practice*, second ed. Addison-Wesley Publishing Company, Reading, Massachusetts, 1990.

[17] FRIEBEL, M., AND MEINKE, M. Model function to calculate the refractive index of native hemoglobin in the wavelength range of 250-1100nm dependent on concentration. *J. Biomed. Opt. 11*, 3 (2006), 034021–1–034021–10.

[18] FRIEBEL, M., ROGAN, A., MÜLLER, G., AND MEINKE, M. Determination of optical properties of human blood in the spectral range 250 to 1100nm using Monte Carlo simulations with hematocrit-dependent effective scattering phase functions. *J. Biomed. Opt. 45*, 12 (2006), 2838–2842.

[19] FRISVAD, J., CHRISTENSEN, N., AND JENSEN, H. Computing the scattering properties of participating media using lorenz-mie theory. *ACM T. Graphic 26*, 3 (2007), 60:1–60:10.

[20] GHARAHBAGHIAN, L., MASSOUDIAN, B., AND DIMASSA, G. Methemoglobinemia and sulfhemoglobinemia in two pediatric patients after ingestion of hydroxylamine sulfate. *Western J. Emergency Med. X*, 3 (2009), 197–201.

[21] GREENBERG, D., ARVO, J., LAFORTUNE, E., TORRANCE, K., FERWERDA, J., WALTER, B., TRUMBORE, B., SHIRLEY, P., PATTANAIK, S., AND FOO, S. A framework for realistic image synthesis. In *SIGGRAPH* (1997), pp. 477–494.

[22] GUTIERREZ, D., SERON, F., A.MUNOZ, AND ANSON, O. Viasualizing underwater ocen optics. *Comput. Graph. Forum*, 2 (2008), 547–556.

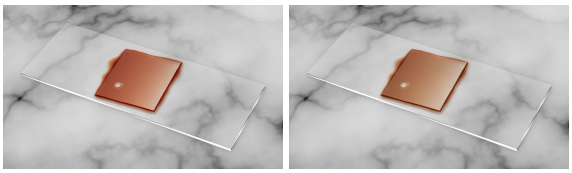

Figure 18: Images illustrating the appearance of blood samples containing abnormal amounts of dysfunctional hemoglobins. Left: 70% methemoglobin and $HCT = 0.4$. Right: 70% sulfhemoglobin and $HCT = 0.4$.

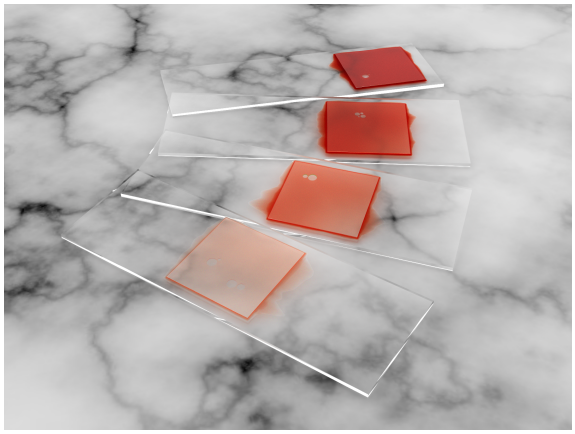

Figure 19: Image of blood samples showing chromatic and translucency changes caused by different HCT values. From front to back: 0.05, 0.15, 0.35 and 0.49.

[23] HAMMER, M., YAROSLAVSKY, A., AND SCHWEITZER, D. A scattering phase function for blood with physiological haematocrit. *Phys. Med. Biol. 46* (2001), N65–N69.

[24] HAMMERLEY, J., AND HANDSCOMB, D. *Monte Carlo Methods*. Wiley, New York, 1964.

[25] HAYMOND, S., CARIAPPA, R., EBY, C., AND SCOTT, M. Laboratory assessment of oxygenation in methemoglobinemia. *Clin. Chem. 51*, 2 (2005), 434–444.

[26] HENTSCHEL, B., TEDJO, I., PROBST, M., WOLTER, M., BEHR, M., BISCHOF, C., AND KUHLEN, T. Interactive blood damage analysis for ventricular assist devices. *IEEE T. Vis. Comput. Gr. 14*, 6 (2008), 1515–1522.

[27] HIRKO, R., FRETTERD, R., AND LONGINI, R. Application of the diffusion dipole to modelling the optical characteristics of blood. *Med. Biol. Eng. 13* (1975), 192–195.

[28] JAKOB, W., ARBREE, A., MOON, J., BALA, K., AND MARSCHNER, S. A radiative transfer framework for rendering materials with anisotropic structure. *ACM T. Graphic 29*, 4 (2010), 53:1–53:13.

[29] KIMMEL, B. SPLITS: A spectral light transport for sand. Master's thesis, School of Computer Science, University of Waterloo, Canada, 2005.

[30] KIMMEL, B., AND BARANOSKI, G. A novel approach for simulating light interaction with particulate materials: application to the modeling of sand spectral properties. *Opt. Express 15*, 15 (2007), 9755–9777.

[31] KINNUNEN, M., KAUPPILA, A., KARMENYAN, A., AND MYLLYLÄ, R. Effect of the size and shape of a red blood cell on elastic light scattering properties. *Biomed. Opt. Express 2*, 7 (2011), 1803–1814.

[32] KISELEV, M., GRYZUNOV, I., AND KOMAROVA, M. Size of human serum albumin molecule in solution. *Biofizika 46*, 3 (2001), 423–7.

[33] KRAMER, K., ELAM, J., SAXTON, G., AND JR., W. E. Influence of oxygen saturation, concentration and optical depth upon the red and near-infrared light transmittance of whole blood. *Am. J. Physiology 165* (1951), 229–246.

[34] KRISHNASWAMY, A., AND BARANOSKI, G. A biophysically-based spectral model of light interaction with human skin. *Comput. Graph. Forum 23*, 3 (2004), 331–340.

[35] LAM, M., AND BARANOSKI, G. A predictive light transport model for the human iris. *Comput. Graph. Forum 25*, 3 (2006), 359–368.

[36] LATIMER, P. A wave-optics effect which enhances light absorption by chlorophyll *in vivo*. *Appl Spectrosc. 40*, 2 (1984), 193–199.

[37] LEE, V., AND TARASSENKO, L. Absorption and multiple scattering by suspensions of aligned red blood cells. *J. Opt. Soc. Am. A. 8*, 7 (1991), 1135–1141.

[38] LEWIS, S., BAIN, B., AND BATES, I. *Dacie and Lewis Practical Hematology*, 10th ed. Churchill Livinstone Elsevier, Philadelphia, PA, USA, 2006.

[39] LINDBERG, L., AND ÖBERG, P. Optical properties of blood in motion. *Opt. Eng. 32*, 2 (1993), 253–257.

[40] LOVELL, A. T., HEBDEN, J. C., GOLDSTONE, J. C., AND COPE, M. Determination of the transport scattering coefficient of red blood cells [3597-121]. In *Society of Photo-Optical Instrumentation Engineers (SPIE) Conference Series* (1999), B. Chance, R. R. Alfano, and B. J. Tromberg, Eds., vol. 3597, p. 175.

[41] MARIEB, E., WILHELM, P., AND MALLATT, J. *Human Anatomy*, 6th ed. Pearson Benjamin Cummings, San Francisco, CA, USA, 2011.

[42] MARTIN, W., COHEN, E., FISH, R., AND SHIRLEY, P. Practical ray tracing of trimmed NURBS surface. *J. Graph, gpu and games tools 5*, 1 (2000), 27–52.

[43] MCCARTNEY, E. *Optics of the Atmosphere: Scattering by Molecules and Particles*. John Wiley & Sons Inc., 1976.

[44] MEINKE, M., GERSONDE, I., FRIEBEL, M., HELFMANN, J., AND MÜLLER, G. Chemometric determination of blood parameters using visible-near-infrared spectra. *Appl. Spectroscp. 59*, 6 (2005), 826–835.

[45] MEINKE, M., MËLLER, G., FRIEBEL, M., AND HELFMANN, J. Optical properties of platelets and blood plasma and their influence on the optical behavior of whole blood in the visible to near infrared wavelength range. *J. Biomed. Opt. 12*, 1 (2007), 014024–1–014024–9.

[46] MOSALIGANTI, K., MACHIRAJU, R., HUANG, K., AND LEONE, G. Geometry-driven visualization of microscopic structures in biology. *Comput. Graph. Forum 27*, 3 (2008), 871–878.

[47] MÜLLER, M., SCHIRM, S., AND TESCHNER, M. Interactive blood simulation for virtual surgery based on smoothed particle hydrodynamics. *Technol. Health Care 12*, 1 (2004), 25–31.

[48] NILSSON, A., ALSHOLM, P., KARLSSON, A., SWARTLING, J., AND ANDERSSON-ENGELS, S. T-matrix computations of light scattering by red blood cells. Tech. Rep. CODEN:LUTEDX(TEAT-7068)/1-24, Lund Institute of Technology, Sweden, 1998.

[49] NILSSON, A., LUCASSEN, G., VERKRUYSSE, W., AND ANDERSON-ENGELS, S. Changes in the optical properties of human whole blood *in vitro* due to slow heating. *Appl Spectrosc. 65*, 2 (1997), 366–373.

[50] NORTHAM, L., AND BARANOSKI, G. A novel first principles approach for the estimation of the sieve factor of blood samples. *Opt. Express 18*, 7 (2010), 7456–7468.

[51] OSHIMA, S., AND SANKAI, Y. Development of red blood cell-photon simulator for optical propagation analysis in blood using Monte Carlo method. *IEEE T. Inf. Technol. B. 15*, 3 (2011), 356–363.

[52] PALMER, K., AND WILLIAMS, D. Optical properties of water in the near infrared. *J. Opt. Soc. Am. 64* (August 1974), 1107–1110.

[53] PETERSCH, B., AND HONIGMANN, D. Blood flow in its context: Combining 3d b-mode and color doppler ultrasonic data. *IEEE T. Vis. Comput. Gr. 13*, 4 (2007), 748–757.

[54] PITTMAN, R. N. *In vivo* photometric analysis of hemoglobin. *Ann Biomed. Eng. 14*, 2 (1986), 1416–1432.

[55] PRAHL, S. *Light Transport in Tissue*. PhD thesis, The University of Texas at Austin, USA, December 1988.

[56] PRAHL, S. Optical absorption of hemoglobin. Tech. rep., Oregon Medical Laser Center, Portland, Oregon, U.S.A, 1999.

[57] QIN, J., PANG, W., NGUYEN, B., NI, D., AND CHUI, C. Particle-based simulation on blood flow vessel wall interactions in virtual surgery. In *Symposium on Information and Communication Technology - SOICT'10* (Hannoi, Vietnam, 2010), pp. 128–133.

[58] RANDEBERG, L., BONESR⊘NNING, J., DALAKER, M., NELSON, J., AND SVAASAND, L. Methemoglobin formation during laser induced photothermolysis of vascular skin lesions. *Lasers in Surgery and Medicine 34* (2004), 414–419.

[59] RENKIN, E. Multiple pathways to capillaary permeability. *Circulation Research 41*, 6 (1977), 735–743.

[60] ROGAN, A., FRIEBEL, M., DÖRSCHEL, K., HAHN, A., AND MÜLLER, G. Optical properties of circulating human blood in the wavelength range 400-2500nm. *J. Biomed. Opt. 4*, 1 (1999), 36–46.

[61] R.SHARP, ADAMS, J., MACHIRAJU, R., LEE, R., AND CRANE, R. Physics-based subsurface visualization of human tissue. *IEEE T. Vis. Comput. Gr. 13*, 3 (2007), 620–629.

[62] SARDAR, D., AND LEVY, L. Optical properties of whole blood. *Laser Med. Sci. 13* (1998), 106–111.

[63] SEGRET, J., JACKSON, R., ANDREWS, E., AND MARCHESI, V. Human erythrocyte membrane glycoprotein: a re-evaluation of the molecular weight as determined by SDS polyacrylamide gel electrophoresis. *Biochem. Bioph. Res. Co. 44*, 2 (1971), 390–395.

[64] SEREBRENNIKOVA, Y. M., SMITH, J. M., HUFFMAN, D. E., LEPARC, G. F., AND GARCÍA-RUBIO, L. H. Quantitative interpretations of visible-nir reflectance spectra of blood. *Opt. Express 16*, 22 (2008), 18215–18229.

[65] SKALAK, R., ZARDA, A. T. R., AND CHIEN, S. Strain energy function of red blood cell membranes. *Biophysical Journal 13* (1973), 245–264.

[66] STEINKE, J., AND SHEPHERD, A. P. Diffusion model of the optical absorbance of whole blood. *J. Opt. Soc. Am. A. 5*, 6 (1988), 813–822.

[67] TONG, X., WANG, J., LIN, S., GUO, B., AND SHUM, H.-Y. Modeling and rendering of quasi-homogeneous materials. *ACM T. Graphic 24*, 3 (2005), 1054–1061.

[68] TSINOPOULOS, S., AND POLYZOS, D. Scattering of He-Ne laser light by an average-sized red blood cell. *Appl. Optics 38*, 25 (1999), 5439–5510.

[69] TYCKO, D., METZ, M., EPSTEIN, E., AND GRINBAUM, A. Flow-cytometric light scattering measurement of red blood cell volume and hemoglobin concentration. *Appl. Optics 24*, 9 (1985), 1355–1365.

[70] VÄLISUO, P., KAARTINEN, I., TUCHIN, V., AND ALANDER, J. New closed-form approximation for skin chromophore mapping. *J. Biomed. Opt. 16*, 4 (2010), 046012–1–046012–10.

[71] WOLAK, E., BYERLY, F., MASON, T., AND CAIRNS, B. Methemoglobinemia in critically ill burned patients. *Am. J. Crit. Care 14*, 2 (2005), 104–108.

[72] WRIEDT, T., HELLMERS, J., EREMINA, E., AND SCHUH, R. Light scattering by single erythrocyte: comparison of different methods. *J.Phys. D. Appl. Phys. 100* (2006), 444–456.

[73] YAMAGUCHI, M., MITSUI, M., MURAKAMI, Y., FUKUDA, H., OHYAMA, N., AND KUBOTA, Y. Multispectral color imaging for dermatology: application in inflammatory and immunologic diseases. In *13th Color Imaging Conference* (Scottsdale, AZ, USA, 2005), pp. 52–58.

[74] YAROSLAVSKY, A., YAROSLAVSKY, I., GOLDBACH, T., AND SCHWARZMAIER, H. Influence of the scattering phase function approximation on the optical properties of blood determined from the integrating sphere measurements. *J. Biomed. Opt. 4*, 47 (1999), 47–53.

[75] YAROSLAVSKY, A. N., PRIEZZHEV, A. V., RODRIQUEZ, J., YAROSLAVSKY, I. V., AND BATTARBEE, H. Optics of blood. In *Handbook of Optical Biomedical Diagnostics* (Bellingham, 2002), V. V. Tuchin, Ed., SPIE-Press, pp. 169–216.

[76] YARYNOVSKA, I. H., AND BILYI, A. Absorption spectra of sulfhemoglobin derivatives of human blood. In *Optical Diagnostics and Sensing VI - SPIE* (2006), G. Cotê and A. Priezzhev, Eds., vol. 6094, pp. 1–6.

Appendix A. Cross-sectional Area of a Red Blood Cell

All possible orientations of RBCs can be represented by giving the direction that their minor axis is facing. Accordingly, the orientation of a RBC with its major axis lying on the XY-plane would have the orientation $[0, 0, 1]$. Let $\vec{\omega}$ be the direction that the cell is being viewed. The CLBlood model requires the calculation of the cross-sectional area of the RBC as viewed from $\vec{\omega}$, *i.e.*, $G(\vec{u}, \vec{\omega})$. To derive a closed formula for $G(\vec{u}, \vec{\omega})$, note that the NURBS shape used is symmetrical. That is, the only variable that affects $G(\vec{u}, \vec{\omega})$ is the inclination angle, ψ, between $\vec{u}$ and $\vec{\omega}$.

If $\psi = 0$, then $G(\vec{u}, \vec{\omega})$ is the cross-sectional area as viewed from above, γ_2. If $\psi = \pi/2$, then $G(\vec{u}, \vec{\omega})$ is the cross-sectional area as viewed from the side, δ_1. For ψ between 0 and $\pi/2$, $G(\vec{u}, \vec{\omega})$ is given by a linear combination of γ_1 and γ_2. That is:

$$G(\vec{u}, \vec{\omega}) = \alpha\gamma_1 + \beta\gamma_2. \tag{16}$$

To determine the variables, α and β, a Monte Carlo technique was used to calculate $G(\vec{u}, \vec{\omega})$ for ψ in range $[0, \pi/2]$ [29]. This experiment showed that $\alpha = 1 - \cos\psi$ and $\beta = \cos\psi$ result in a good agreement between the faster analytical method and the Monte Carlo technique (Figure 20). Therefore, we employ the following expression for the cross-sectional area of the red blood cell viewed from $\vec{\omega}$:

$$G(\vec{u}, \vec{\omega}) = \gamma_1(1 - \cos\psi) + \gamma_2 \cos\psi. \tag{17}$$

A.1. Determining the Average Cross-Sectional Areas

With NURBS, we are able to create a bounding volume for the RBC as well as perform ray intersections. This allows us to use a standard Monte Carlo rejection sampling technique to determine the average cross-sectional areas of the RBC viewed from the side and from the top, denoted by γ_1 and γ_2, respectively. This is done offline to increase performance.

To compute the cross-sectional area, we first create a bounding sphere for the NURBS representation. Then we cast rays towards the bounding sphere, where the rays originate from a disc. This disc should be perpendicular to the ray direction as well as have the same radius as the bounding sphere. The origin of each ray is selected randomly from a point on the disc and an intersection test is performed to determine

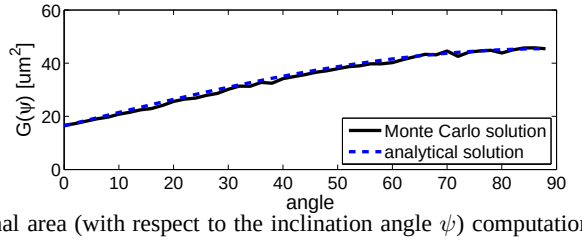

Figure 20: Comparison of cross-sectional area (with respect to the inclination angle ψ) computations performed using the selected Monte Carlo technique and the corresponding analytical formula.

whether the ray hit the NURBS model. N number of rays is cast and the total number of rays that intersected the NURBS model, num, is recorded. The cross-sectional area as viewed from the direction of the rays can then be calculated as:

$$\text{Cross-sectional Area} = num/N * A_{disc}, \tag{18}$$

where A_{disc} is the area of the disc. Therefore, we can compute γ_1 by casting the rays to the side profile of the RBC. Similarly, we can compute γ_2 by casting the rays to the top profile of the RBC.

A.2. Determining Volume of the NURBS model

To compute the volume of the NURBS model, a similar technique to the one used in Appendix A.1 was used. A bounding box for the NURBS model was computed. Then N number of points was randomly sampled in the bounding box and the total number of random points sampled inside the NURBS model, num, was recorded. The volume of the NURBS model can then be calculated as:

$$V = num/N * V_{BoundingBox}, \tag{19}$$

where $V_{BoundingBox}$ is the volume of the bounding box used.

Appendix B. Cross-sectional Area per Unit Volume

In this section, we derive formulas for $K(\vec{\omega})$, the cross-sectional area per unit volume for a ray traveling in the direction of $\vec{\omega}$), with respect to three common distributions of red blood cell orientations, namely random, aligned and rolling, with respect to one axis.

Randomly distributed orientation refers to a situation where all the RBCs' orientations are distributed according to a random uniform distribution, *i.e.*, all cell orientations have an equal probability. In contrast, when the RBCs have an aligned orientation distribution, all RBCs have the same orientation. Rolling refers to the case where all the RBCs are rotating about the same axis. In this scenario, RBCs are rotated around the axis randomly with an uniform distribution.

B.1. Random Case

Given the hematocrit, H, and the volume per RBC, MVC, the density of all the RBCs is given by $\delta = H/MVC$. The quantity $n(\vec{u})$ is defined as density of RBCs with the orientation $\vec{u}$. If the distribution of the orientations of the RBCs is completely random with equal probability of any possible orientation, then $n(\vec{u})$ must be a constant. Furthermore, since δ is the density of all RBCs, the sum of $n(\vec{u})$ for all orientations must be equal to δ. Therefore,

$$\delta = \int_{\Omega} n(\vec{u}) d\Omega \tag{20}$$

and

$$n(\vec{u}) = \frac{\delta}{4\pi}. \tag{21}$$

Finally, plugging Equations 20 and 21 into Equation 5 gives:

$$
\begin{aligned}
K_{random}(\vec{\omega}) &= \int_{\Omega} n(\vec{u})G(\vec{u},\vec{\omega})d\Omega \\
&= \int_0^{2\pi}\int_0^{\pi} \frac{\delta}{4\pi}(\gamma_1(1-|\cos\psi|)+\gamma_2|\cos\psi|)\sin\psi d\psi d\phi \\
&= \frac{\delta}{4\pi}\int_0^{2\pi}\int_0^{\pi}(\gamma_1+(\gamma_2-\gamma_1)|\cos\psi|)\sin\psi d\psi d\phi \\
&= \frac{\delta}{4\pi}\left(\gamma_1\int_0^{2\pi}\int_0^{\pi}\sin\psi d\psi d\phi\right)\left((\gamma_2-\gamma_1)\int_0^{2\pi}\int_0^{\pi}|\cos\psi|\sin\psi d\psi d\phi\right) \\
&= \frac{\delta}{4\pi}\left(\gamma_1 2\pi[-\cos\psi]_0^{\pi}+(\gamma_2-\gamma_1)\left(\int_0^{2\pi}d\phi\right)\left(2\int_0^{\pi/2}\cos\psi\sin\psi d\psi\right)\right) \\
&= \frac{\delta}{4\pi}\left(4\pi\gamma_1+(\gamma_2-\gamma_1)(4\pi)\int_0^{\pi/2}\frac{1}{2}\sin(2\psi)d\psi\right) \\
&= \frac{\delta}{4\pi}\left(4\pi\gamma_1+(\gamma_2-\gamma_1)(4\pi)\frac{1}{2}[-\frac{1}{2}\cos(2\psi)]_0^{\pi/2}\right) \\
&= \frac{\delta}{4\pi}\left(4\pi\gamma_1+(\gamma_2-\gamma_1)\pi[-\cos(2\psi)]_0^{\pi/2}\right) \\
&= \frac{\delta}{4\pi}(4\pi\gamma_1+(\gamma_2-\gamma_1)2\pi) \\
&= \frac{\delta}{4\pi}(4\pi\gamma_1+2\pi\gamma_2-2\pi\gamma_1) \\
&= \frac{\delta}{4\pi}(2\pi\gamma_1+2\pi\gamma_2) \\
&= \frac{\delta}{2}(\gamma_1+\gamma_2). \qquad (22)
\end{aligned}
$$

B.2. Rolling Case

When the cells are only rolling along one axis, then the formula for K and G must be adjusted accordingly. Because we are using ray-tracing techniques, we can derive K considering the RBCs rotating around their local x-axis in object coordinate system, and then perform the necessary object to world transformation to place the RBCs in world coordinate system [16].

Similarly to the previous case, $G(\vec{u},\vec{\omega})$ is the same as the one given by Equation 17, with the exception that γ_2, the cross-sectional area viewed from the top, is no longer a constant. It is dependent on the rotation angle θ, which corresponds to the angle that the current RBC has been rotated about the x-axis. We denote $\gamma_2'(\theta)$ as the θ dependent version of the cross-sectional area viewed from the top. This results in the following expression for $G_{rolling}$:

$$G_{rolling}(\vec{u},\vec{\omega}) = \gamma_1(1-|\cos\psi|)+\gamma_2'(\theta)|\cos\psi|, \qquad (23)$$

where γ_1 is still the cross-sectional area as viewed from the side (*i.e.*, the thinner profile of the RBC).

Note that $\gamma_2'(\theta)$ is equal to $G(\vec{u},\vec{\omega})$, which gives:

$$\gamma_2'(\theta) = \gamma_1(1-|\cos\theta|)+\gamma_2|\cos\theta|. \qquad (24)$$

Finally, replacing Equation 24 into Equation 23 yields the following expression for $G_{rolling}$:

$$G_{rolling}(\vec{u},\vec{\omega}) = \gamma_1(1-|\cos\psi|)+(\gamma_1(1-|\cos\theta|)+\gamma_2|\cos\theta|)|\cos\psi|. \qquad (25)$$

If all the cells are rolling, then there is an equal probability of the cell having $\theta = [0, 2\pi]$, which gives:

$$\delta = \int_{\Omega} n(\vec{u})d\Omega \qquad (26)$$

and

$$n(\vec{u}) = \frac{\delta}{2\pi}. \qquad (27)$$

After obtaining expressions for $n(\vec{u})$ and $G_{rolling}(\vec{u},\vec{\omega})$, we can plug them into Equation 5 and derive $K_{rolling}$:

$$
\begin{aligned}
K_{rolling}(\vec{\omega}) &= \int_{\Omega} n(\vec{u})G(\vec{u},\vec{\omega})d\Omega \qquad (28)\\
&= \int_0^{2\pi} \frac{\delta}{2\pi}(\gamma_1(1-|\cos\psi|)+(\gamma_1(1-|\cos\theta|)+\gamma_2|\cos\theta|)|\cos\psi|)d\theta\\
&= \frac{\delta}{2\pi}\left(\int_0^{2\pi}\gamma_1(1-|\cos\psi|)d\theta+\int_0^{2\pi}(\gamma_1(1-|\cos\theta|)+\gamma_2|\cos\theta|)|\cos\psi|)d\theta\right)\\
&= \frac{\delta}{2\pi}\left(\gamma_1(1-|\cos\psi|)\int_0^{2\pi}d\theta+|\cos\psi|\int_0^{2\pi}(\gamma_1(1-|\cos\theta|)+\gamma_2|\cos\theta|)d\theta\right)\\
&= \frac{\delta}{2\pi}\left(\gamma_1(1-|\cos\psi|)(2\pi)+|\cos\psi|\int_0^{2\pi}\gamma_1+(\gamma_2-\gamma_1)|\cos\theta|d\theta\right)\\
&= \frac{\delta}{2\pi}\left(\gamma_1(1-|\cos\psi|)(2\pi)+|\cos\psi|\left(\gamma_1\int_0^{2\pi}d\theta+(\gamma_2-\gamma_1)\int_0^{2\pi}|\cos\theta|d\theta\right)\right)\\
&= \frac{\delta}{2\pi}\left(\gamma_1(1-|\cos\psi|)(2\pi)+|\cos\psi|\left(2\pi\gamma_1+(\gamma_2-\gamma_1)(4)\int_0^{\pi/2}\cos\theta d\theta\right)\right)\\
&= \frac{\delta}{2\pi}\left(\gamma_1(1-|\cos\psi|)(2\pi)+|\cos\psi|\left(2\pi\gamma_1+4(\gamma_2-\gamma_1)[\sin\theta]_0^{\pi/2}\right)\right)\\
&= \frac{\delta}{2\pi}\left(\gamma_1(1-|\cos\psi|)(2\pi)+|\cos\psi|\left(2\pi\gamma_1+4\gamma_2-4\gamma_1\right)\right)\\
&= \frac{\delta}{2\pi}\left(\gamma_1(1-|\cos\psi|)(2\pi)+|\cos\psi|\left((2\pi-4)\gamma_1+4\gamma_2\right)\right)\\
&= \delta\gamma_1(1-|\cos\psi|)+\frac{\delta}{2\pi}(\gamma_1(2\pi-4)+4\gamma_2)|\cos\psi|. \qquad (29)
\end{aligned}
$$

We can also define $K_{rolling}$ with respect to the axis that the RBCs are rotating around, *i.e.*, the x-axis. Let β be the angle between x-axis, $\vec{a}$, and $\vec{\omega}$. We remark that $\beta = \pi/2 - \theta$. Then $\cos\theta = \sin\beta$. Therefore, $K_{rolling}$ can also be represented by:

$$K_{rolling}(\vec{\omega}) = \delta\gamma_1(1-|\sin\beta|)+\frac{\delta}{2\pi}(\gamma_1(2\pi-4)+4\gamma_2)|\sin\beta|. \qquad (30)$$

B.3. Alignment Case

For the case where all RBCs have the same orientation, we have $n(\vec{u}) = \delta$. We remark that in this case $G(\vec{u},\vec{\omega})$ is also given by Equation 17 as the derivation is still applicable, *i.e.*, the cell shape is the same, γ_1 and γ_2 correspond to the same cross-sectional areas viewed from the side and top respectively, and the only factor that affects $G(\vec{u},\vec{\omega})$ is the inclination angle. Furthermore, since all RBCs have the same orientation, there is no need to integrate over the domain of all possible orientations to derive K. Accordingly, $K_{aligned}$ is given by:

$$K_{aligned}(\vec{\omega}) = n(\vec{u})G(\vec{u},\vec{\omega}) = \delta(\gamma_1(1-|\cos\psi|)+\gamma_2|\cos\psi|). \qquad (31)$$

Appendix C. Probability Distribution Function for Orientation

As mentioned in Section 4.3, the orientation of the cell must be selected from the set of all orientations that were considered while generating the distance to the cells. This procedure takes into the probability distribution function (PDF) derived for each case such that orientations that have a larger $G(\vec{u},\vec{\omega})$ have a higher probability of being selected. Details on the derivations and sampling of these PDFs are provided in the following subsections.

C.1. Random Case

In this case, all possible orientations need to be considered. The orientation, $\vec{u}$, of the cell can be separated into two parameters: polar angle ψ with respect to the ray direction, $\vec{\omega}$, and azimuthal angle ϕ with respect to the plane perpendicular to $\vec{\omega}$. Starting with Equation 11, we obtain:

$$
\begin{aligned}
p_{random}(\psi,\phi) &= p(\vec{u})\\
&= \frac{G(\vec{u},\vec{\omega})}{\int_{\vec{u}} G(\vec{u},\vec{\omega})\mathrm{d}\vec{u}}\\
&= \frac{G(\vec{u},\vec{\omega})}{\int_0^{2\pi}\int_0^{\pi} G(\vec{u},\vec{\omega})\sin\psi\mathrm{d}\psi\mathrm{d}\phi}\\
&= \frac{G(\vec{u},\vec{\omega})}{2\pi\int_0^{\pi} G(\vec{u},\vec{\omega})\sin\psi\mathrm{d}\psi}. \qquad (32)
\end{aligned}
$$

We then proceed to obtain the marginal density functions for ϕ and ψ. The marginal density fucntion for ϕ is given by:

$$\begin{aligned} p_{random}(\phi) &= p_{randomAzimuthal}(\phi) \\ &= \int_0^{\pi} p_{random}(\psi,\phi)\sin\psi \mathrm{d}\psi \\ &= \int_0^{\pi} \frac{G(\vec{u},\vec{\omega})}{2\pi\int_0^{\pi} G(\vec{u},\vec{\omega})\sin\psi\mathrm{d}\psi}\sin\psi\mathrm{d}\psi \\ &= \frac{1}{2\pi\int_0^{\pi} G(\vec{u},\vec{\omega})\sin\psi\mathrm{d}\psi}\int_0^{\pi} G(\vec{u},\vec{\omega})\sin\psi\mathrm{d}\psi \\ &= \frac{1}{2\pi}. \end{aligned} \tag{33}$$

To sample ϕ from an uniform PDF in the range of 0 to 2π, one can employ Algorithm 2, where ξ_{10} represents a random number uniformly distributed in the interval $[0, 1]$.

Algorithm 2 Sampling $p_{random}(\phi)$.

$\phi_R \leftarrow 2\pi\xi_{10}$

The marginal density function for ψ is given by:

$$\begin{aligned} p_{random}(\psi) &= p_{randomPolar}(\psi) \\ &= \frac{p_{random}(\psi,\phi)}{p_{randomAzimuthal}(\phi)} \\ &= \frac{2\pi G(\vec{u},\vec{\omega})}{2\pi\int_0^{\pi} G(\vec{u},\vec{\omega})\sin\psi\mathrm{d}\psi} \\ &= \frac{\gamma_1(1-|\cos\psi|)+\gamma_2|\cos\psi|}{\int_0^{\pi}(\gamma_1+(\gamma_2-\gamma_1)|\cos\psi|)\sin\psi\mathrm{d}\psi} \\ &= \frac{\gamma_1(1-|\cos\psi|)+\gamma_2|\cos\psi|}{\gamma_1\int_0^{\pi}\sin\psi\mathrm{d}\psi+(\gamma_2-\gamma_1)\int_0^{\pi}|\cos\psi|\sin\psi\mathrm{d}\psi} \\ &= \frac{\gamma_1(1-|\cos\psi|)+\gamma_2|\cos\psi|}{\gamma_1[-\cos\psi]_0^{\pi}+2(\gamma_2-\gamma_1)\int_0^{\pi/2}\cos\psi\sin\psi\mathrm{d}\psi} \\ &= \frac{\gamma_1(1-|\cos\psi|)+\gamma_2|\cos\psi|}{\gamma_1(2)+2(\gamma_2-\gamma_1)\int_0^{\pi/2}\frac{1}{2}\sin(2\psi)\mathrm{d}\psi} \\ &= \frac{\gamma_1(1-|\cos\psi|)+\gamma_2|\cos\psi|}{2\gamma_1+(\gamma_2-\gamma_1)[-\frac{1}{2}\cos(2\psi)]_0^{\pi/2}} \\ &= \frac{\gamma_1(1-|\cos\psi|)+\gamma_2|\cos\psi|}{2\gamma_1+(\gamma_2-\gamma_1)} \\ &= \frac{\gamma_1(1-|\cos\psi|)+\gamma_2|\cos\psi|}{\gamma_1+\gamma_2}. \end{aligned} \tag{34}$$

For simplicity, we use rejection sampling to sample this PDF. It was implemented using Algorithm 3 and considering random random numbers ξ_{11} and ξ_{12} uniformly distributed in the interval $[0, 1]$.

Algorithm 3 Rejection sampling for $p_{random}(\psi)$.

if $\gamma_1 > \gamma_2$ **then**
  max $\leftarrow \gamma_1$
else
  max $\leftarrow \gamma_2$
end if
max $\leftarrow$ max / $(\gamma_1 + \gamma_2)$
repeat
  $\psi \leftarrow \pi\xi_1$
until max $* \xi_2 \leq p_{randomPolar}(\psi)\sin\psi$

C.2. Rolling Case

In the case, the orientation of the cell is fixed except for its rotation, represented by the angle θ, about $\vec{a}$, the rotation axis. Once again, we start with Equation 11, and substitute G by Equation 23, the cross-sectional area associated with the rolling cells case. This results in:

$$\begin{aligned}
p_{rolling}(\theta) &= \frac{G(\vec{u},\vec{\omega})}{\int G(\vec{u},\vec{\omega})\mathrm{d}\theta} \\
&= \frac{\gamma_1(1-|\sin\beta|)+(\gamma_1(1-|\cos\theta|)+\gamma_2|\cos\theta|)|\sin\beta|}{\int_0^{2\pi}\gamma_1(1-|\sin\beta|)+(\gamma_1(1-|\cos\theta|)+\gamma_2|\cos\theta|)\sin\beta d\theta} \\
&= \frac{\gamma_1(1-|\sin\beta|)+(\gamma_1(1-|\cos\theta|)+\gamma_2|\cos\theta|)|\sin\beta|}{\gamma_1(1-|\sin\beta|)\int_0^{2\pi}\mathrm{d}\theta+|\sin\beta|\int_0^{2\pi}\gamma_1+(\gamma_2-\gamma_1)|\cos\theta|\mathrm{d}\theta} \\
&= \frac{\gamma_1(1-|\sin\beta|)+(\gamma_1(1-|\cos\theta|)+\gamma_2|\cos\theta|)|\sin\beta|}{\gamma_1(1-|\sin\beta|)2\pi+|\sin\beta|\left(\gamma_1\int_0^{2\pi}\mathrm{d}\theta+(\gamma_2-\gamma_1)(4)\int_0^{\pi/2}\cos\theta\mathrm{d}\theta\right)} \\
&= \frac{\gamma_1(1-|\sin\beta|)+(\gamma_1(1-|\cos\theta|)+\gamma_2|\cos\theta|)|\sin\beta|}{\gamma_1(1-|\sin\beta|)2\pi+|\sin\beta|\left(2\pi\gamma_1+4(\gamma_2-\gamma_1)[\sin\theta]_0^{\pi/2}\right)} \\
&= \frac{\gamma_1(1-|\sin\beta|)+(\gamma_1(1-|\cos\theta|)+\gamma_2|\cos\theta|)|\sin\beta|}{\gamma_1(1-|\sin\beta|)2\pi+|\sin\beta|\left(\gamma_1(2\pi-4)+4\gamma_2\right)}.
\end{aligned} \tag{35}$$

We also use rejection sampling to sample this PDF. It was implemented using Algorithm 4 and considering random random numbers ξ_{13} and ξ_{14} uniformly distributed in the interval $[0,1]$.

Algorithm 4 Rejection sampling for $p_{rolling}(\theta)$.

```
if γ1 > γ2 then
    max ← γ1
else
    max ← γ2
end if
max ← max / γ1(1 − |sin β|)2π + |sin β| (γ1(2π − 4) + 4γ2)
repeat
    θ ← 2πξ13
until max ∗ ξ14 ≤ p_rolling(θ)
```

C.3. Alignment Case

When all the cells are aligned to an orientation, represented by $\vec{U}$, selecting the orientation becomes trivial. The orientation is always $\vec{U}$. The resulting PDF is then given by:

$$p_{aligned}(\vec{u}) = \begin{cases} 1 & \text{if } \vec{u}=\vec{U} \\ 0 & otherwise \end{cases} \tag{36}$$